Title

Iron isotope fractionation at the core–mantle boundary by thermodiffusion

Journal

Nature Geoscience, 13(5)

ISSN

1752-0894

Authors

Lesher, Charles E
Dannberg, Juliane
Barfod, Gry H
et al.

Publication Date

2020-05-01

DOI

10.1038/s41561-020-0560-y

Peer reviewed

nature geoscience

SUPPLEMENTARY INFORMATION

https://doi.org/10.1038/s41561-020-0560-y

In the format provided by the authors and unedited.

Iron isotope fractionation at the core–mantle boundary by thermodiffusion

Charles E. Lesher[1,2,3] ✉, Juliane Dannberg[2,4], Gry H. Barfod[1], Neil R. Bennett[2], Justin J. G. Glessner[3], Daniel J. Lacks[5] and James M. Brenan[6]

[1]Department of Geoscience, Aarhus University, Aarhus, Denmark. [2]Department of Earth and Planetary Sciences, University of California, Davis, CA, USA. [3]Interdisciplinary Center for Plasma Mass Spectrometry, University of California, Davis, CA, USA. [4]Department of Geological Sciences, University of Florida, Gainesville, FL, USA. [5]Department of Chemical and Biomolecular Engineering, Case Western Reserve University, Cleveland, OH, USA. [6]Department of Earth and Environmental Sciences, Dalhousie University, Halifax, Nova Scotia, Canada. ✉e-mail: lesher@geo.au.dk

SUPPLEMENTARY INFORMATION FOR

IRON ISOTOPE FRACTIONATION AT THE CORE-MANTLE BOUNDARY BY THERMODIFFUSION

Charles E. Lesher[1,2,3*], Juliane Dannberg[2,4], Gry H. Barfod[1], Neil R. Bennett[2], Justin J. G. Glessner[3], Daniel J. Lacks[5], and James M. Brenan[6]

1. Department of Geoscience, Aarhus University, Aarhus, Denmark
2. Department of Earth and Planetary Sciences, University of California, Davis, California, USA
3. Interdisciplinary Center for Plasma Mass Spectrometry, University of California, Davis, California, USA
4. Department of Geological Sciences, University of Florida, Gainesville, Florida, USA
5. Department of Chemical and Biomolecular Engineering, Case Western Reserve University, Cleveland, Ohio, USA
6. Department of Earth and Environmental Sciences, Dalhousie University, Halifax, Nova Scotia, Canada

*corresponding author; lesher@geo.au.dk

Constraints on the Fe isotope composition of Earth's silicate mantle

It has been known for some time that mantle-derived magmas (basalts) are on average enriched in heavy Fe isotopes relative to chondrites[1-3] (Fig. S1), and that the development of this geochemical trait is in large part the consequence of partial melting and fractional crystallization processes[4-6]. We summarize the arguments for this below.

Iron in the silicate mantle occurs as ferrous Fe^{2+} and ferric Fe^{3+} with the latter behaving more incompatibly, i.e. preferentially enriched in the silicate liquid relative to solids, during partial melting and subsequent magmatic differentiation (at least prior to FeTi oxide saturation). Ferric iron, having higher field strength than Fe^{2+}, tends to favor tetrahedral coordination with oxygen while ferrous iron is commonly octahedrally coordinated in minerals. Melting occurs as a result of a difference in the force constant for Fe in these two coordination states. The higher force constant for Fe in tetrahedral coordination concentrates heavier Fe isotopes on these sites, while at equilibrium octahedrally coordinated Fe tends to be isotopically lighter. These relationships have been illuminated by Mössbauer and, more recently, by nuclear resonant inelastic X-ray scattering studies of minerals and silicate glasses[7,8] showing that for basaltic systems the force constant is ~200 N m^{-1} for Fe^{2+} and 350 N m^{-1} for Fe^{3+}, although presently values for basaltic melts rely on data for silicate glasses.

To place constraints on the Fe isotope composition of the silicate mantle we begin by first considering the available data for normal, transitional and enriched mid-ocean ridge basalts (MORB) compiled by Sossi et al.[6] and summarized in Fig. S1. Here, the kernel density distribution (in blue) with a bandwidth of 0.01 ‰ for the 44 MORB samples yields an average δ^{57}Fe of 0.160 ± 0.012 ‰ (± 95% confidence interval) referenced to the Fe metal standard IRMM014. This spectrum of compositions is considered representative of melts derived from the upper mantle variably influenced by source heterogeneity and crystal fractionation involving olivine ± clinopyroxene ± plagioclase.

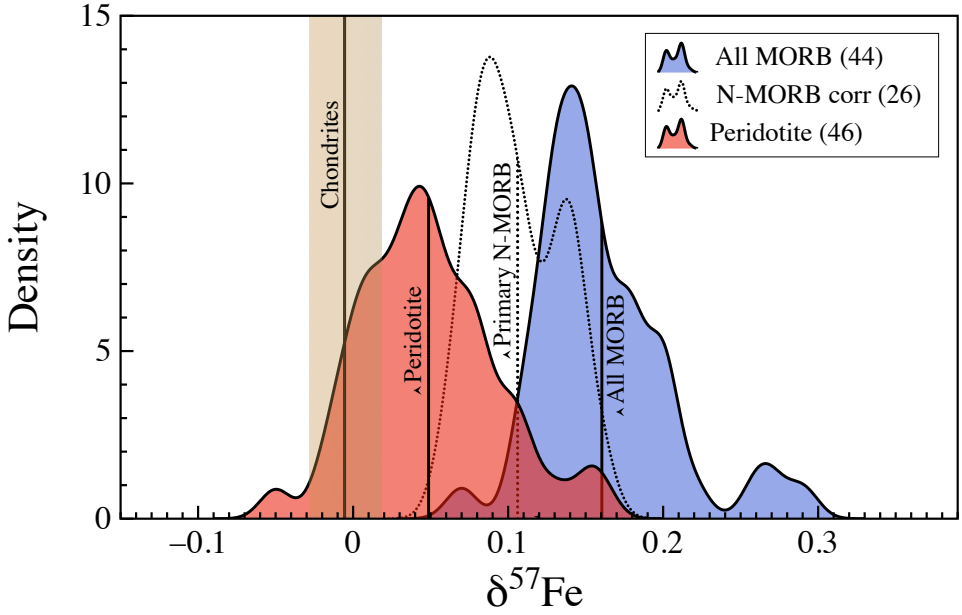

Figure S1. Kernel density distribution (bandwidth = 0.010) for δ^{57}Fe (in per mil) for normal, transition and enriched MORBs and peridotites (abyssal samples and continental xenoliths) compiled by Sossi et al.[6] (see reference for primary data sources). The dashed distribution is for primary mantle melts back-correcting the suite of normal (N-)MORB for olivine fractionation to a mantle Mg# of 0.895 and assuming $\Delta\delta^{57}Fe_{ol\text{-}melt} = -0.15$[6]. Vertical lines within each distribution are average δ^{57}Fe, i.e. 0.160 ± 0.012 ‰, 0.106 ± 0.011 ‰ and 0.044 ± 0.014 ‰, (± is the 95% confidence interval) for "(#)" samples of MORBs, N-MORBs used to estimated primary melts and peridotites, respectively. The vertical band is the average δ^{57}Fe for carbonaceous, ordinary and enstatite chondrites, i.e. 0.006 ± 0.022 ‰ (± 2σ)[9].

The density distribution in red (Fig. S1) is for abyssal peridotites and continental xenoliths taken as most representative of upper mantle lherzolite with an average δ^{57}Fe of 0.044 ± 0.014 ‰. Also, shown in Fig. S1 is the average δ^{57}Fe for carbonaceous, ordinary and enstatite chondrites, i.e. 0.006 ± 0.022 ‰ (± 2σ), reported by Craddock and Dauphas[9] and commonly taken to represent the bulk Earth value[8,10]. Fig. S1 shows that there is more than a 0.15 ‰ spreading in δ^{57}Fe between assumed bulk Earth and MORB. Including ocean island and arc basalts for comparison[11] would not change this finding, although these latter data are not as tightly clustered as MORB, undoubtedly reflecting their more complex petrogenesis. Ocean island basalts (OIB) are especially germane to the present discussion, but constraining the Fe isotope composition of the source from lavas is exacting given the complexity of melting a lithologically heterogeneous plume mantle. While this must be considered on a case by basis case – which is beyond the scope of this paper – prime targets for such an analysis are OIBs with high $^{3}He/^{4}He$ and Fe/Mn ratios, and negative ^{182}W anomalies

suggesting that the source for these mantle plumes interacted with the outer core[12-16]. Presently, the most robust constraints on the core contributions come from W isotopes placing an upper limit of 0.2 wt. %[15] to 0.8 wt. %[16] core material in OIBs possessing the most negative ^{182}W anomalies, e.g., Hawaii, Somoa, Reunion and the Azores. More uncertain is the degree of coupling of W (and other highly siderophile elements) and Fe during core–mantle interaction given the differences in compatibility in mantle silicates.

To understand the overall spread in $\delta^{57}Fe$ shown in Fig. S1 it is essential to consider the effects of partial melting and crustal processes, specifically, crystal fractionation. We begin with the latter. Since MORBs are the product of magmatic differentiation beneath oceanic spreading centers, the effects of crystal fractionation must be reversed to constrain plausible compositions of primary mantle melts. Sossi et al.[6] estimated the Fe isotopic compositions of primary melts of a lherzolitic source by back-correcting normal MORB for low pressure olivine fractionation in an iterative fashion until model melts reached equilibrium with mantle olivine ($Fo_{89.5}$), assuming an olivine–melt Fe isotope fractionation factor ($\Delta\delta^{57}Fe_{ol\text{-}melt}$) of -0.15 ‰ consistent with the literature[5,17]. The Sossi et al. model results, presented in Fig. S1 as the dashed line distribution with an average $\delta^{57}Fe$ of 0.106 ± 0.011 ‰, shows that an ~0.05 ‰ increase of $\delta^{57}Fe$ in MORB can be produced by differentiation of primary mantle melts. Similar results have been reported by other authors[8] indicating that only about half the difference between MORBs and peridotites results from crystal fractionation.

A further consideration is the effects of partial melting to produce primary MORB melts. For example, Sossi et al. constructed simple equilibrium and fractional melting models for a mantle lherzolite having a $Fe^{3+}/\Sigma Fe = 0.037$ and assuming that Fe^{3+} is an order of magnitude more incompatible than Fe^{2+} during melting. Using published force constants[8] for Fe^{2+} and Fe^{3+} and mass balance constraints, Sossi et al.[6] predict that primary MORB melt produced by 10-20% partial melting would be ~0.05 ‰ more enriched in ^{57}Fe (relative to ^{54}Fe) than the source, while the residue of melting would be depleted by ~0.01 ‰. These calculations strongly depend on redox conditions, the relative compatibility of Fe^{2+} and Fe^{3+} during melting, and the force constants for Fe species, yet the parameters used by Sossi et al.[6] are well justified and favorable to producing Fe isotopic fractionation during melting. As such, $\Delta\delta^{57}Fe_{\text{Primitive MORB melt - residue}} \sim +0.06$ can be reasonably taken as an upper limit during

melting of a lherzolitic source. It should be emphasized that this does not include possible effects of source heterogeneity, melt percolation and reactive flow and metasomatism[18], or of kinetic effects operating on grain scales[19] that could further amplify or erase fractionations arising from melting and differentiation. Furthermore, authors have questioned the reliability of peridotites to constrain the silicate mantle due to metasomatic overprinting and secondary alteration[6,20].

To the extent that the subset of lherzolites screened for these effects are representative of the upper mantle[6] and the modeling of crystal fractionation and partial melting are robust, the δ^{57}Fe of the MORB source is ~0.045 ‰ and distinct from chondrites. If the Fe isotope composition of the MORB source is representative of the silicate mantle as a whole and the bulk Earth is near-chondritic we must look to other processes to explain the isotopic shift. This leads us to two final considerations: core segregation and impact-related vaporization during formation of the Moon.

Both core formation and impacts could leave their imprint on the silicate mantle. However, most studies have shown that the fractionation factors for Fe isotopes between putative core and silicate phases are very small at high P and T and, if at all, the heavier Fe isotopes concentrate in the metallic phase that would leave the silicate mantle isotopically light[7,21-23]. This sense of fractionation might be reversed if C or H is abundant in the core, but not if O is the light element responsible for the outer core's density deficit[24]. Consequently, core formation at the high pressure and temperature conditions for the early Earth is not expected to impart appreciable Fe isotope fractionation relative to a primitive silicate mantle. Furthermore, impact-related vaporization, while expected to enrich the gaseous phase in light isotopes and enriching the condensed phases in heavier isotopes, is also difficult to assess for the Earth–Moon system in part because of uncertainties in the composition of the Earth's core, mantle and likewise bulk composition, and because we lack good constraints on the bulk composition of the Moon.

Like terrestrial basalts, lunar basalts are elevated in δ^{57}Fe, often to greater extent than terrestrial basalts, but the roles, for example, of ilmenite in the formation of high Ti basalts and fractionation of olivine for low Ti basalts leave open the possibility that the Moon is

near-chondritic in Fe isotope composition[25], consistent with other non-traditional stable isotopes, i.e. Si, Mg, Ti, etc. with volatilities similar to Fe. If this is the case and the silicate mantle of Earth is slightly enriched in heavy Fe isotopes, then this latter feature could have developed after the formation of the Moon. Such conjecture is speculative and mentioned to emphasize the difficulty in establishing with certainty the bulk Fe isotopic composition of the Earth and Moon. MORBs provide us with the most robust observations, and correcting for crystal fractionation and partial melting predict that the MORB source is slightly enriched in Fe isotopes relative to chondrites. This property of the silicate mantle is not readily explained by core formation and may originate from impact processes, but it is also prudent to explore other possible causes for the enrichment. It is in this context that we investigate the potential for thermodiffusion to fractionate Fe isotopes in the vicinity of the core–mantle boundary of the Earth, and assess whether any of this fractionated material entrained by plume upwelling reaches the upper mantle on geological time scales where it could be involved in basalt generation.

Thermodiffusion experiments

Experimental methods

Thermodiffusion experiments on Fe - Fe alloy melts are performed in a standard ½" piston-cylinder apparatus with an assembly consisting of a straight-wall graphite heater surrounded by an insulating sleeve of barium carbonate wrapped in Pb-foil and containing MgO filler rod. This assembly has a large temperature gradient along its longitudinal axis well-suited for thermodiffusion studies (Fig. S2). Powdered starting material is packed into a 1 mm diameter bore drilled into MgO rod placed into the lower half of the assembly

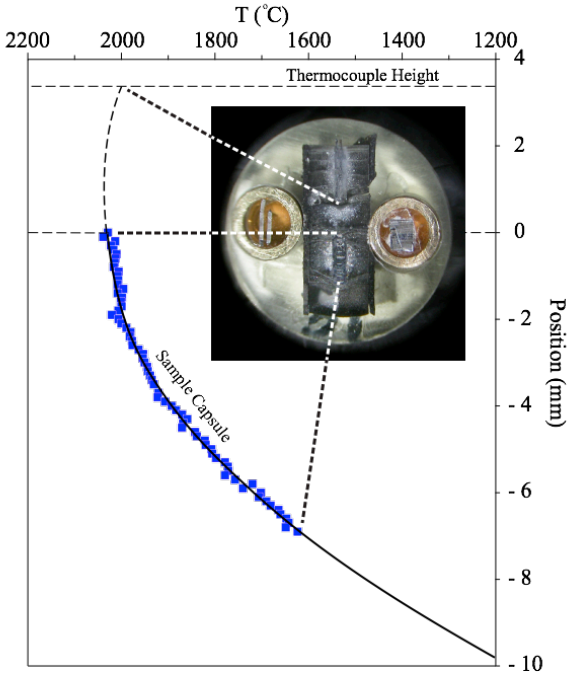

Figure S2. Temperature profile along the longitudinal axis of the piston cylinder assembly used for the thermodiffusion experiments on Fe – Fe alloy melts determined by the spinel growth kinetics technique[26]. Inserted picture shows the sectioned and polished interior portions of the assembly for run SOR-12 (graphite heater, MgO filler rod and capsule and thermocouple + sheath) mounted in epoxy together with ¼" round mounts containing LA-MC-ICP-MS standards IRRM-014 Fe wire (right) and Alfa Fe foil (left). The dashed lines connect positions along the length of the assembly with positions along the measured temperature profile. (Figure modified after Brenan and Bennett[27].)

with the top of the sample capsule located ~2 mm below the middle of the graphite furnace. The temperature gradient within the sample capsule was calibrated by Brenan and Bennett[27] using the spinel growth kinetics model[26] where a tube of high purity alumina enclosing a Pt wire is inserted into the sample bore producing a longitudinal interface between the outer surface of the alumina tube and surrounding MgO. The spinel layer forms at this interface at high temperature and pressure. Variation in the thickness of the spinel layer is used to constrain the temperature gradient that varies from ~7 K mm^{-1} near the mid-point of the assembly to ~85 K mm^{-1} at 5 mm from the mid-point (Fig. S2). The longitudinal temperature profile through the sample under normal operating conditions is shown in Figure S1 together with a photomicrograph of a sectioned and polished assembly together with Fe standards mounted for laser ablation ICP-MS analysis. The capsule containing the sample has an inner bore diameter of 1 mm and length of 3 to 5.5 mm. During an experiment the temperature is measured with a C- type ($W_{95}Re_5$-$W_{74}Re_{26}$) thermocouple positioned ~3.5 mm above the top

of the sample capsule and about equidistant from the midpoint (hot spot) of the furnace. We target a temperature 2273 ± 7 K for the hot end of the capsule and estimate temperatures elsewhere using a polynomial fit to the calibration data in Fig. S2. The temperature difference between hot and cold ends of the capsule range from 190 to 265 K (depending on capsule length) and the average temperature within the capsule is estimated to be 2209 ± 27 K.

All experiments were performed at 2 GPa. Assemblies were pressurized cold and annealed at 1073 K for 12-24 hrs, followed by ramping at 100 K min^{-1} to the final dwell conditions, i.e. ~2273 K at the hot end. Temperature was controlled during the ramp phase and for ~10 mins at the final dwell temperature with a standard feedback loop, after which the run was switched to manual mode in order to maintain constant power consumption. This was done chiefly as a precaution should the thermocouple drift or fail entirely during the run. While there were no thermocouple failures running at close to 2273 K, during the course of the longer experiments we found a downward drift in temperature (≤ 3%, relative) at constant power consumption. We do not believe this was due to recrystallization of the pressure medium, but rather progressive contamination of the thermocouple either from interdiffusion between the wire alloys at their junction or impurities coming from the surrounding medium[28].

Finally, the extent of isotopic fractionation by thermodiffusion during heating to the set point temperature was evaluated. Because temperature varies across the capsule, while ramping to the set point temperature melting progresses downwards from the hot end until the entire charge is molten. As such it is possible that some isotope fractionation by thermodiffusion could develop on heating to the set point temperature. At our ramp rate of 100 K min^{-1} it takes about 4 mins after crossing the solidus (~1845 K for pure Fe at 2 GPa[29]) to reach the set point temperature of ~2273 K. SOR-32 was quenched immediately on reaching the set point temperature and analyzed in the same manner as the other experiments. As shown in Table S1 within analytical uncertainties there is no resolvable Fe isotopic variation. Based on these results we assume for all the experiments that t = 0 and $\Delta\delta^{56,57}Fe_{cold\text{-}hot} = 0$ at the moment the thermocouple temperature reaches the target dwell temperature. Experiments were conducted for up to 77.5 mins and quenched at ~500 K s^{-1} by cutting power to the furnace.

Analytical methods and results

Spatial variations in Fe isotope composition in run products were determined using a NewWave Research *UP 213* (213nm wavelength) laser configured with the small internal volume *SuperCell* sample chamber coupled to a MC-ICP-MS (*Nu Plasma HR*) at the Interdisciplinary Center for Plasma Mass Spectrometry (UC Davis). Each charge was laser-ablated with a series of parallel line traverses 500 μm long, oriented perpendicular to the temperature gradient. We employed a 20 - 40 μm diameter laser beam moving at 10 μm s^{-1} with a repetition rate of 10 Hz and energy density of 3.5 - 5 J cm^{-2}. Ablated material in the *SuperCell* was carried away from the sample surface in a He gas stream (0.7 L min^{-1}) and transported to a 30 mL PFA chamber where it is mixed with Ar (1 L min^{-1}) before transfer to the sample injector of the ICP torch.

HR MC-ICP-MS measurements were conducted in pseudo-high mass resolution using 0.05 mm wide source slit and alpha slits deployed to 50% beam transmission optimizing with our Fe in house std. This enabled resolution ($m/\Delta m$) of 8000-9000 (measured from peak scans) that avoided spectral interferences from isobaric argide and oxide species ($^{40}Ar^{14}N^{+}$ on $^{54}Fe^{+}$, $^{40}Ar^{16}O^{+}$ on $^{56}Fe^{+}$ and $^{40}Ar^{16}OH^{+}$ on $^{57}Fe^{+}$). ^{53}Cr was monitored to correct for the isobaric interferences of ^{54}Cr on ^{54}Fe. We alternated sample measurements with analysis of the IRMM014 Fe reference standard (metal wire) and calculated delta values for unknowns by the standard-sample-standard bracketing method[30-32]. High purity (99.999%) *Alfa* Fe foil was run before and after each sample block. Twenty-three replicate analyses of *Alfa* Fe foil gave $\delta^{56}Fe$ of 0.09 ± 0.69 ‰ (2 S.D.). To assess the precision and accuracy of our LA-MC-ICP-MS analysis, we processed an aliquot of *Alfa* Fe using traditional anion-exchange chromatography methods and analyzed the solution by MC-ICP-MS as detailed below. The $\delta^{56}Fe$ is 0.051 ± 0.037 (2σ) and within uncertainty of that obtained by laser ablation.

As a crosscheck of our laser ablation results we sampled material from the hot end, cold end and mid-section of one charge (SOR-27; $FeNi_5$) using a precision microdrill (courtesy of T. Waight, Copenhagen U). The powdered aliquots were digested in hot concentrated HF-HNO_3 for 24 hrs in sealed Savillex® PFA containers, followed by dry-down and several oxidizing-evaporation steps first in HNO_3 and then HCl - H_2O_2 mixtures prior to ion

exchange chromatography. Fe was eluted by anion-exchange chromatography using PFA Teflon columns containing 0.25 ml Bio-Rad AG MP-1, 100-200 mesh resin[33]. Purified Fe samples were then reconstituted in 2 % HNO_3 and measured by MC-ICP-MS in dry plasma mode using a *DSN-100* interfaced with the MC-ICP-MS torch. Each sample analysis included four or more replicate measurements with reproducibility of <0.05 ‰ (2 S.D.) for δ^{56}Fe and <0.07 ‰ (2 S.D.) for δ^{57}Fe. In-house standard UI Fe was run before and after each sample block (3-4 samples) giving a long-term reproducibility ±0.05 ‰ for δ^{56}Fe and ±0.08 ‰ for δ^{57}Fe. All our analytical results over multiple analytical sessions are presented in Table S1. Session-to-session reproducibility is reflected in the coherence of the isotopic gradient of a given run representing data gathered during a number of sessions separated by months.

Table S1 presents experimental thermodiffusion data for four bulk compositions, i.e., pure Fe, $FeNi_1$, $FeNi_5$ and $FeNi_{10}S_{15}Cu_1$. With the exception of run SOR-32 using pure Fe and quenched immediately after reaching the dwell temperature (the null experiment described above), all the experiments produced measurable Fe isotope fractionation with ^{57}Fe and ^{56}Fe enriched at the cold end relative to ^{54}Fe. Figure S3 shows the correlation of δ^{56}Fe and δ^{57}Fe together with reference lines having slopes of 1.47 and 1.49 as predicted for equilibrium and kinetic mass-dependent fractionation, respectively[34]. Deviation of the measurements from either mass-dependent reference line is well within analytical uncertainty. For pure Fe, $\Delta\delta^{57}Fe_{cold\text{-}hot}$ is 4.36 ‰ after 15 mins (SOR-30), 6.59 ‰ after 20 mins (SOR-33), and 8.23 ‰ after 30 mins (SOR-29). Likewise, $\Delta\delta^{57}Fe_{cold\text{-}hot}$ for $FeNi_1$ after 40 mins (SOR-6) is 4.40 ‰, while $\Delta\delta^{57}Fe_{cold\text{-}hot}$ for $FeNi_5$ after 10 mins (SOR-25) is 4.52 ‰ and after 30 mins (SOR-27) is 8.71 ‰. The largest isotope fractionation ($\Delta\delta^{57}Fe_{cold\text{-}hot}$ = 11.09 ‰) is produced in molten $FeNi_{10}S_{15}Cu_1$ after 73 mins (SOR-12). There is no resolvable relative fractionation of Fe and Ni in any of the alloy melts, while Fe and S are strongly fractionated from one another in $FeNi_{10}S_{15}Cu_1$ alloy liquid with S enriched and Fe depleted at hot end by 15 mol %[27].

Together, these results indicate that the addition of sulfur to FeNi alloy melt enhances Fe isotope fractionation, but we find no influence of Ni in the S-free alloys. This latter finding is consistent with the work of Liu et al.[23] but not with Elardo and Shahar[24] who report a well-resolved Ni dependence for Fe isotope fractionation in metal–silicate equilibration

experiments at 2123 K and 1 GPa. What we cannot ascertain at this time is whether the enhanced fractionation of Fe isotopes in SOR-12 is due to S or simply that thermodiffusion promotes large chemical separation of S from Fe and Ni in alloy liquids, as previously shown[27]. Williams et al.[35] found that troilite (FeS) in iron meteorites is isotopically lighter than the coexisting metal suggesting that the force constant for Fe-S complexes is smaller than for Fe-Fe complexes. To the extent that the interatomic forces in minerals and melts are similar, heavy Fe could be more enriched at the cold end of SOR-12 compared to the S-free experiments simply because Fe-Fe complexes are more abundant there. However, this explanation is not easily reconciled with Shahar et al.'s[36] equilibration experiments involving molten Fe alloy and silicates showing that heavy Fe prefers the alloy and more so at higher S contents. Further work is needed to understand the role of S, but it is noteworthy that Brenan and Bennett[27] found that unlike S, carbon and silicon were not fractionated from Fe by thermodiffusion as is the case for Ni in all of the compositions they studied.

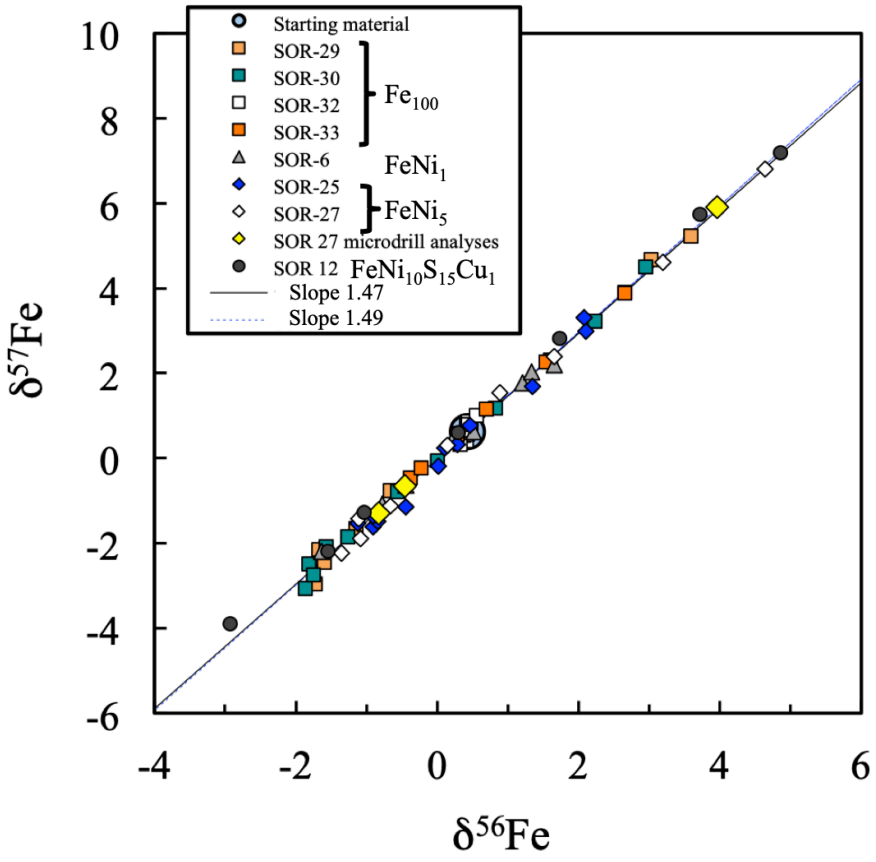

Figure S3. Three – isotope plot showing covariations of ^{54}Fe, ^{56}Fe and ^{57}Fe produced by thermodiffusion for pure Fe (SOR-29, -30, -32 and -33; squares), $FeNi_1$ (SOR-6; triangles), $FeNi_5$ (SOR-25, -27; diamonds) and $FeNi_{10}S_{15}Cu_1$ (SOR-12; circles). The large yellow diamonds are isotopic values determines by solution MC-ICP-MS for micro-drilled material from the hot, middle and cold portions of SOR-27. The starting material is shown by the large circle (reflecting uncertainties) enclosing all of the data for SOR-32 quenched immediately on reaching the final dwell conditions. The solid and dashed curves have slopes of 1.47 and 1.49 predicted for equilibrium and kinetic mass-dependent fractionation, respectively[34].

Table S1. Fe isotope data for starting material and for experimental run products measured at various positions along temperature gradients by laser ablation (*in-situ*) and solution (*micro-drilled material*) MC-ICP-MS.

	Position (mm)	*T (K)*	*[a]δ⁵⁶Fe*	*[b]error*	*[a]δ⁵⁷Fe*	*[b]error*	*[c]LA-MC-ICP-MS analytical session [Roman numerals] or by Solution MC-ICP-MS*
Fe starting material			0.43	0.03	0.63	0.19	*Solution*
			Fe₁₀₀				
SOR-32	0.00	2290	0.41	0.11	0.83	0.12	*V*
t_{dwell} = *0 min*	0.05	2290	0.29	0.07	0.57	0.06	*VI*
	0.44	2292	0.48	0.05	0.81	0.05	*VII*
	0.68	2291	0.41	0.06	0.40	0.09	*V*
	1.31	2284	0.44	0.14	0.69	0.09	*V*
	1.98	2268	0.38	0.04	0.55	0.03	*V*
	2.02	2267	0.41	0.03	0.55	0.18	*VI*
	2.41	2253	0.46	0.16	0.62	0.10	*VII*
	2.63	2244	0.45	0.04	0.86	0.09	*V*
	3.29	2211	0.33	0.07	0.33	0.10	*V*
	4.50	2129	0.45	0.12	0.67	0.08	*VI*
	4.60	2121	0.44	0.03	0.79	0.12	*V*
	4.75	2109	0.55	0.09	1.01	0.04	*VI*
	[d]Est. BC	*2235*	*0.44*	*[c]0.13*	*0.65*	*[c]0.38*	

SOR-30	0.00	2268	-1.58	0.01	-2.08	0.12	*IV*
t_{dwell} = *15 min*	0.59	2247	-1.26	0.16	-1.85	0.13	*IV*
	1.14	2223	-0.57	0.04	-0.78	0.04	*IV*
	1.73	2190	0.00	0.00	-0.06	0.06	*IV*
	2.24	2157	0.83	0.06	1.19	0.08	*IV*
	2.87	2109	2.23	0.05	3.22	0.15	*IV*
	3.11	2089	2.95	0.14	4.51	0.11	*IV*
	[d]*Est. BC*	*2193*	*0.37*		*0.59*		
SOR-33	0.00	2282	-0.38	0.06	-0.47	0.07	*VII*
t_{dwell} = *20 min*	1.41	2274	-0.23	0.01	-0.22	0.09	*VII*
	2.10	2257	0.28	0.00	0.56	0.02	*VII*
	2.72	2235	0.70	0.02	1.16	0.24	*VII*
	3.39	2202	1.54	0.02	2.26	0.21	*VII*
	4.05	2163	2.65	0.01	3.89	0.06	*VII*
	[d]*Est. BC*	*2246*	*0.46*		*0.74*		
SOR-29	0.00	2270	-1.73	0.30	-2.96	0.01	*III*
t_{dwell} = *30 min*	0.45	2264	-1.60	0.24	-2.46	0.00	*III*
	0.93	2254	-1.14	0.10	-1.65	0.23	*III*
	1.83	2223	-0.67	0.29	-0.76	0.17	*III*
	2.51	2190	0.43	0.04	0.56	0.04	*III*
	3.19	2149	1.60	0.15	2.30	0.10	*III*
	3.81	2105	2.65	0.33	3.90	0.01	*III*

	4.14	2079	3.03	0.04	4.67	0.11	*III*
	4.44	2054	3.58	0.07	5.24	0.24	*III*
	[d]*Est. BC*	*2190*	*0.37*		*0.56*		
				FeNi$_1$			
SOR-6	0.00	2256	-1.63	0.10	-2.19	0.33	*I*
t_{dwell} = 40 min	0.85	2243	-0.78	0.11	-1.09	0.20	*I*
	1.52	2225	-0.45	0.13	-0.63	0.11	*I*
	2.36	2192	0.22	0.28	0.46	0.38	*I*
	2.85	2168	0.52	0.19	0.63	0.53	*I*
	3.07	2157	1.20	0.11	1.78	0.08	*I*
	3.20	2149	1.33	0.34	2.04	0.75	*I*
	3.36	2140	1.66	0.46	2.21	0.90	*I*
	[d]*Est. BC*	*2212*	*0.26*		*0.40*		
				FeNi$_5$			
SOR-25	0.00	2282	-1.12	0.16	-1.53	0.30	*II*
t_{dwell} = 10 min	0.70	2276	-0.44	0.09	-1.14	0.01	*II*
	1.47	2258	0.11	0.11	0.24	0.07	*II*
	1.51	2256	0.02	0.05	-0.18	0.10	*II*
	2.09	2235	0.29	0.12	0.34	0.07	*II*
	2.44	2219	0.46	0.10	0.76	0.10	*II*
	2.75	2203	1.34	0.04	1.69	0.25	*II*
	3.54	2156	2.10	0.06	2.99	0.15	*II*

	3.66	2148	2.08	0.24	3.30	0.21	*II*
	[d]*Est. BC*	*2235*	*0.39*		*0.42*		
SOR-27	0.00	2277	-1.08	0.12	-1.89	0.21	*II*
t_{dwell} = *30 min*	0.75	2275	-1.35	0.16	-2.23	0.13	*II*
	1.50	2262	-1.10	0.06	-1.42	0.11	*II*
	2.14	2243	-0.66	0.14	-1.11	0.11	*II*
	2.86	2213	0.15	0.38	0.30	0.38	*II*
	3.53	2176	0.89	0.06	1.55	0.19	*II*
	4.10	2138	1.66	0.47	2.40	1.03	*II*
	4.77	2086	3.20	0.12	4.61	0.08	*II*
	5.43	2029	4.64	0.14	6.82	0.11	*II*
	[d]*Est. BC*	*2197*	*0.50*		*0.71*		
Micro-drilled/solution analysis							
	Top (hot)	~2262	-0.83	0.10	-1.30	0.14	*Solution*
	Intermediate	~2233	-0.45	0.06	-0.64	0.11	*Solution*
	Bottom (cold)	~2057	3.96	0.07	5.91	0.25	*Solution*

			FeNi$_{10}$ S$_{15}$Cu$_1$				
SOR-12	0.00	1994	-2.92	0.16	-3.90	0.19	*I*
t_{dwell} = *73 min*	1.01	1974	-1.55	0.25	-2.20	0.34	*I*
	1.64	1952	-1.04	0.04	-1.28	0.26	*I*
	2.52	1910	0.30	0.07	0.61	0.09	*I*
	3.37	1856	1.73	0.09	2.82	0.25	*I*
	4.16	1795	3.71	0.11	5.75	0.03	*I*
	4.77	1742	4.85	0.22	7.19	0.40	*I*
	[d]*Est. BC*	*1900*	*0.46*		*0.90*		

[a]$\delta^{57,56}Fe = [(^{57,56}Fe/^{54}Fe)_{sample}/(^{57,56}Fe/^{54}Fe)_{IRMM\text{-}14}\text{-}1]$ x1000 (per mil)

[b]Uncertainties reported for solution analyses are two standard deviations (2σ) based on 6-8 std-sample brackets. Uncertainties for laser ablation analyses are one standard deviation (1σ) for each double std-sample bracket, where the sample value is the ratio of signal intensities integrated over the 500 μm laser ablation traverse perpendicular to the longitudinal axis of the charge.

[c]LA-MC-ICP-MS work was carried out during seven separate analytical sessions (I-VII) over a period of 12 months. The null experiment (SOR-32), quenched immediately after reaching the dwell temperature was analyzed repeatedly during three separate sessions (total of 13 analyses) yielding a 2σ of 0.13 and 0.38 for $\delta^{56}Fe$ and $\delta^{57}Fe$, respectively. These uncertainties represent minimum estimates of the uncertainties in bulk composition estimated for the remaining experiments as described in footnote d.

[d]*Est. BC* – Bulk composition estimated by spatial integration of the isotopic composition along the longitudinal axis of the charge. Uncertainties are difficult to quantify, but estimated to be comparable to uncertainties for the null experiment SOR-32.

Time Series

The rise to steady-state isotopic fractionation by thermodiffusion is evaluated by relating the magnitude of the sensitivity fractionation factor[37] (Ω_{Fe}; in units of ‰ K^{-1} amu^{-1}) to experimental run duration, where Ω_{Fe} is found from the change in $\delta^{56,57}Fe$ with T divided by the unit mass difference between the heavy isotope (^{56}Fe or ^{57}Fe) and ^{54}Fe.

Table S2. Experimental parameters and thermodiffusion sensitivity factors (Ω; ‰ K^{-1} amu^{-1}) used in time series study to estimate D_{Fe} using equation S-1. Uncertainties for Ω in parentheses correspond to the trailing digits.

Expt. #	Composition	t (min)	total length (mm)	t(s)/τ	Ω_{Fe56}	Ω_{Fe57}
SOR-32	Fe_{100}	0	4.75	0.00	-	-
SOR-30	Fe_{100}	15	3.11	4.60	0.0126(5)	0.0122(4)
SOR-33	Fe_{100}	20	4.05	3.61	0.0126(3)	0.0120(4)
SOR-29	Fe_{100}	30	4.44	4.51	0.0126(3)	0.0123(4)
SOR-6	$FeNi_1$	40	3.36	10.50	0.0126(9)	0.0116(9)
SOR-25	$FeNi_5$	10	3.66	2.21	0.0110(9)	0.0112(7)
SOR-27	$FeNi_5$	30	5.43	3.01	0.0118(3)	0.0117(3)
SOR-12	$FeNi_{10}S_{15}Cu_1$	73	4.77	9.52	0.0150(7)	0.0147(6)

Values of Ω_{Fe} based on $\delta^{56}Fe$ and $\delta^{57}Fe$ are listed in Table S2. Average values are plotted in Figure S4 as a function of normalized run time, t/τ, where *t* is the elapsed time at the dwell temperature and τ is the characteristic time given by $d^2/\pi^2 D_{Fe}$ with d being the capsule length and D the isotope interdiffusivity or self-diffusivity for Fe. We seek the best fit to the subset of data for $FeNi_{0\text{-}5}$ alloy compositions to constrain D using the relation[38].

$$\Omega_{Fe}(t) = \Omega_{Fe}(ss)\left[1 - e^{\frac{-t}{\tau}}\right] \qquad \text{(S-1)}$$

Ignoring small differences in the diffusivities of ^{54}Fe, ^{56}Fe and ^{57}Fe, the best fit to the data yields $D_{Fe} = 5 \times 10^{-9}$ m^2 s^{-1} for $FeNi_{0\text{-}5}$ alloy melts. This same diffusivity is used to compute the rise time curve for the $FeS_{15}Ni_{10}$ alloy and shows that in both cases a close approach to steady state is achieved within 30 mins for all compositions studied. Figure S4 also provides a comparison of our fit to equation S-1 and the rise time curve predicted by our ASPECT code for the same experimental parameters (see discussion below).

Table S3 lists the steady-state thermodiffusion isotope sensitivity factors Ω_{ss} determined by equation S-1 and dimensionless Chapman-Enskog fractionation factors α_o for metallic liquids

(this study) and silicate melts[39].

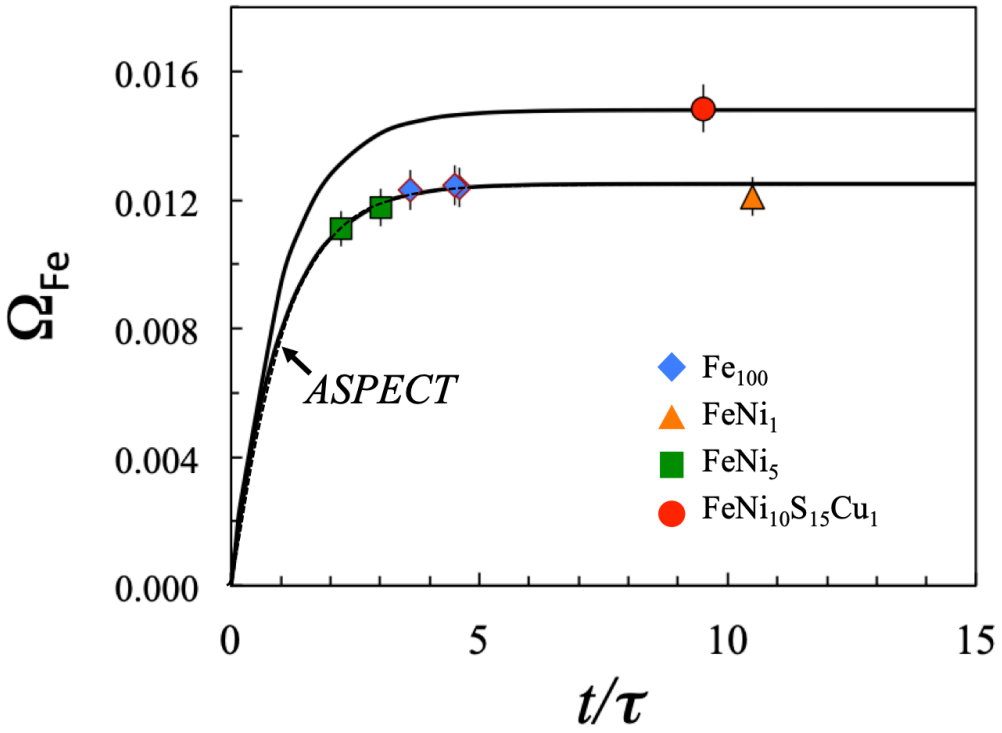

Figure S4. Variation in the average Ω_{Fe} as a function of time expressed as t/τ, where t is the time at the dwell temperature $\tau = d^2/\pi^2 D_{Fe}$. The diffusivity D_{Fe} is found by iterative solution of equation S-1 using values of t and d given in Table S2 to yield the best fit to data for pure Fe, $FeNi_1$ and $FeNi_5$. The resulting rise time curves (solid lines) are for $D_{Fe} = 5 \times 10^{-9}$ m^2 s^{-1}. The dashed curve is the time-dependent isotopic fractionation for the FeNi alloys predicted by our APSECT code using the same diffusivity and α_o of 2.87, as discussed below.

Table S3. Steady-state thermodiffusion isotope sensitivity factor (Ω_{ss})and dimensionless Chapman-Enskog fractionation factor (α_o)for pure Fe and Fe alloy melts (this study) and silicate melts[39]. Uncertainties in parentheses correspond to the trailing digits.

Composition	$^{\#}\Omega_{ss}$	$^{*}\alpha_o$
$Fe_{100-95}Ni_{0-5}$	0.0122(4)	2.96(11)
$Fe_{75}S_{15}Ni_{10}$	0.0148(2)	3.50(15)
Silicate melts	0.0110 - 0.0141	2.09 - 2.82

$^{\#}$Thermodiffusion isotope sensitivity factor (in ‰ K^{-1} amu^{-1}) for the steady-state determined from the best-fit of data present in Table S2 using equation S-1. Estimated uncertainties on the last digit are given in parentheses. Values for silicate melts for mean temperatures of 1700 – 1825 K[39,40].
*The dimensionless Chapman-Enskog fractionation factor α_o constrained by data for either $\delta^{56}Fe$ or $\delta^{57}Fe$ using $\delta^{56,57}Fe(T) - \delta^{56,57}Fe(T_o) = M'\alpha_o\left(\frac{T-T_o}{T_o}\right)$, where $\delta^{56,57}Fe(T)$ and $\delta^{56,57}Fe(T_o)$ are the isotopic compositions (in standard delta notation) for temperature T in K and average temperature T_o in K for the near steady-state experiments SOR-29, -6, -27 and -12. M' is 18.2 for $\delta^{56}Fe$ and 27.0 for $\delta^{57}Fe$. Values for silicate melts ranging from basalt to rhyolite[39].

Modeling

To demonstrate how temperature gradients across the core-mantle boundary can facilitate the fractionation of iron isotopes and lead to possible entrainment of isotopically enriched material, we model this process using the finite-element mantle convection software ASPECT[41,42]. We assume that everywhere in the model where temperatures are above the pure iron solidus, iron isotopes will fractionate following the equation describing thermodiffusion for the simplest case of separation of a mixture of hard spheres of equal size but different masses[39]

$$\frac{\partial C}{\partial t} + \mathbf{u}\cdot\nabla C - \nabla\cdot(D\nabla C) - \nabla\cdot\left(\frac{C(1-C)\alpha' D}{T}\nabla T\right) = 0, \qquad \text{(S-2)}$$

where $C = C^{56,57}Fe/(C^{54}Fe + C^{56,57}Fe)$, $C^{54,56,57}Fe$ is the concentration of ^{54,56,57}Fe, **u** is the velocity, D is the self-diffusivity, T is the temperature and α' [= $(1 - C)^{-1}$ α_o $(m_h - m_l)$ / $(m_h + m_l)$] is the Chapman-Enskog fractionation factor describing how the fractionation depends on temperature, dimensionless α_o (see Table S3), and mass (m) of the heavy (h) and light (l) isotopes. Note that because equation S-2 describes the evolution of the relative concentration of the heavy isotope (instead of the ratio of C_h and C_l), a scaling factor of $(1 - C)^{-1}$ with respect to the value inferred from the experiments is introduced in the definition of α'. In the following treatment we will focus on the evolving distribution of ^{57}Fe. To obtain the transport velocity **u** and the temperature T, ASPECT additionally solves the compressible Stokes equations and the energy conservation equation that together describe convection in the Earth's mantle[42]

$$
\begin{aligned}
-\nabla \cdot \left[2\eta\left(\varepsilon(\mathbf{u}) - \frac{1}{3}(\nabla\cdot\mathbf{u})\mathbf{1}\right)\right] + \nabla p &= \rho\mathbf{g} \\
\nabla\cdot(\rho\mathbf{u}) &= 0 \\
\rho C_p\left(\frac{\partial T}{\partial t} + \mathbf{u}\cdot\nabla T\right) - \nabla\cdot k\nabla T = \; & 2\eta\left(\varepsilon(\mathbf{u}) - \frac{1}{3}(\nabla\cdot\mathbf{u})\mathbf{1}\right) : \left(\varepsilon(\mathbf{u}) - \frac{1}{3}(\nabla\cdot\mathbf{u})\mathbf{1}\right) \\
& + \alpha_{\text{thermal}} T\,(\mathbf{u}\cdot\nabla p)
\end{aligned}
\qquad \text{(S-3)}
$$

Here, η is the viscosity, $\varepsilon(\mathbf{u})$ is the strain rate, p is the pressure, ρ is the density, C_p is the specific heat capacity, k is the thermal conductivity and $\alpha_{thermal}$ is the thermal expansivity. Both adiabatic heating and shear heating are included.

We use second-order finite elements and an implicit, second-order backward differentiation formula time stepping scheme to advect the temperature and the concentration of ^{57}Fe, employing the entropy-viscosity stabilization algorithm[43]. Note that our equations do not include any physical mechanism that describes how much liquid iron would be present in any part of the lowermost mantle that is above the Fe metal solidus, or how it came to be there. We assume that some amount of liquid iron is present, transported there, for example, due to morphological instabilities that cause iron-rich liquid from the outer core to infiltrate into the lowermost mantle as proposed by Otsuka and Karato[44]. Other mechanisms may be involved associated with the increase in wetting behavior of molten iron alloy at lower mantle conditions[45] and transport of metallic melts to the base of the mantle in deeply subducted slabs[46]. We also do not preclude silicate melting in the vicinity of the CMB[47], but do anticipate that any isotopic fractionation occurring will develop most rapidly in the presence of molten iron where ion mobilities are expected to be the greatest.

Benchmark: Reproducing the experimental results

To show that ASPECT solves the equations for thermodiffusion correctly, we generated a model that uses the same setup as our experiments, and then compared the numerical and experimental results. In particular, we used the setup of SOR-27 as given in Table S1, prescribing the (fixed) temperature profile as a quadratic function

$$T = T_0 + T_1\, z + T_2\, z^2 \qquad \text{(S-4)}$$

with T_0 = 2004.39 + 273.15 K, T_1 = 3218.61 K m^{-1}, T_2 = 9.04608 x 10^6 K m^{-2} and z the distance along the capsule (ranging between 0 and 5.43 x 10^{-3} m). The initial composition is C = 0.270162 (implying δ^{57}Fe = +0.6 for the experimental starting material) and the relevant

material properties are $D_{Fe} = 5 \times 10^{-9}$ m^2 s^{-1} (Fig. S3) and $\alpha_o = 2.87$ for SOR-27 (Fig. 2). In addition, we assume that there is no advection in the capsule, setting the velocity **u** to zero. The model evolves for a model time of 2 hrs, after which steady state is reached.

Figure S4 shows the rise time curve predicted for this model agrees with the data and our analytical solution (eq. S-1) used to constrain the diffusivity. A direct comparison of experimental and simulated thermodiffusion profiles for SOR-27 is shown in Figure S5 in the latter case showing the sensitivity of the resulting profile to the choice of α_o.

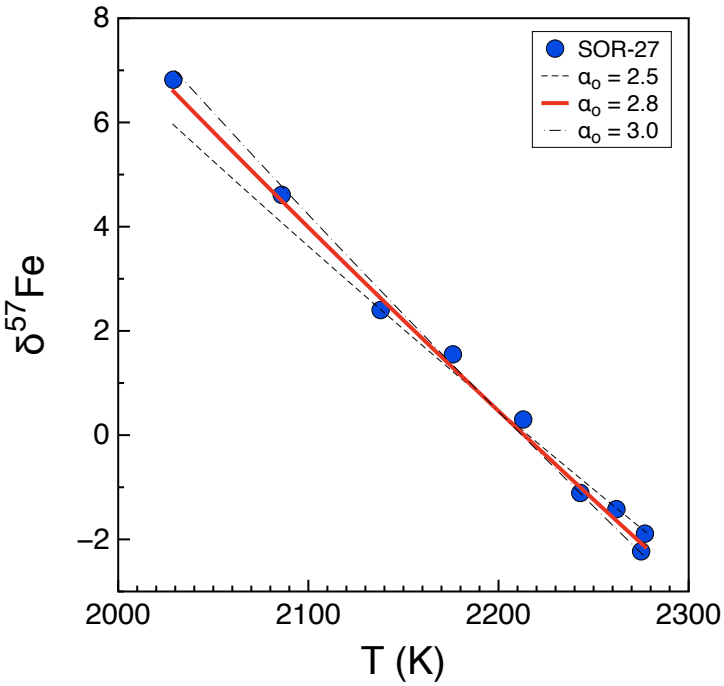

Figure S5. Comparison of experimental thermodiffusion profile for SOR-27 ($FeNi_5$ alloy) and results of our ASPECT model setup with the same initial conditions and run duration and a range of values for α_o.

Application: Thermodiffusion at the core-mantle boundary

To model the fractionation of Fe isotopes near the core-mantle boundary, we use a 2D Cartesian box with extensions of 2900 km x 2900 km (see Figure S6). The temperature is fixed to 3800 K at the core-mantle boundary and 1600 K at the surface, so that the model is heated from below. We omit a thermal boundary layer at the upper boundary and instead prescribe the potential temperature because our model does not include any physical mechanism that would facilitate slab subduction. Otherwise, this cold upper boundary layer would grow to an unrealistic thickness over the model evolution time and inhibit ascent of the plume into the upper mantle where melting will occur. The concentration of ^{57}Fe is fixed to 0.27 (implying δ^{57}Fe = 0) at the bottom boundary, assuming that material in the outer core

is well mixed. This does not preclude stratification at the top of the outer core[48], but in this model we do not consider the possibility of isotopic fractionation in that region. We do note, however, that the thermal structure of a buoyant layer at the top of the core would tend to favor the development of isotopically heavy core material at its top. In this scenario, it is conceivable that core material crossing the CMB into the lowermost mantle would be heavier than we have assumed in our model. This possibility would magnify the isotopic effects we are modeling on the mantle side of the CMB. Stress-free boundary conditions are applied on all model boundaries.

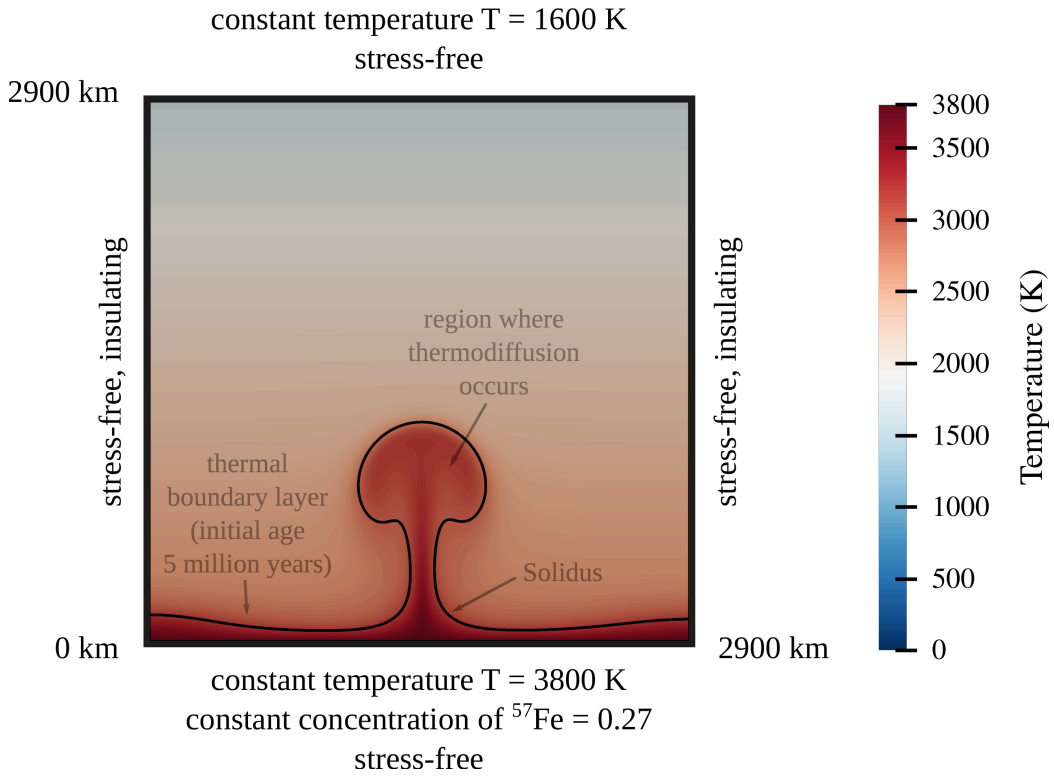

Figure S6. Setup of our ASPECT geodynamic model solving equations S-2 and S-3. Results here are for the simulation after 850 Myrs shown in Fig. S9. Colors represent the temperature in the model and the solid black line traces the iron solidus of Morard et al.[49].

The model starts from a uniform distribution of ^{57}Fe (where $C = 0.27$, corresponding to $\delta^{57}\text{Fe} = 0$) everywhere and an adiabatic temperature profile corresponding to a potential temperature of 1600 K. This implies a temperature contrast of approximately 1070 K at the core-mantle boundary, and we include a thermal boundary layer computed according to the half-space cooling model and an age of 5 million years. The choice of this very young age reflects the assumption that the model starts just after the boundary layer has been depleted by a rising plume or has been swept away by a subducting slab, presumably the most

favorable conditions (that is, steepest thermal gradient) for the fractionation of the iron isotopes. In either case the ASPECT model is tracking the evolution of the thermal boundary layer just above the CMB that periodically becomes unstable and spawns plume upwelling. In addition, we add a small Gaussian-shaped temperature perturbation of 10^{-4} K in the center of the bottom boundary to control the position at which the first plume forms.

As we are focused on core-mantle boundary processes, we have deliberately simplified the model setup, choosing most material properties as constants. Exceptions are the density ρ and the viscosity η, which both depend on temperature and pressure via

$$\eta = \eta_0 \exp(-b\,(T - T_{adi}) / T_{adi}) \qquad \text{(S-5)}$$

and

$$\rho = \rho_0\,(1 - \alpha_{thermal}(T-T_{adi})\,)\,\exp(\kappa P) \qquad \text{(S-6)}$$

The reference viscosity is chosen as $\eta_0 = 5 \times 10^{22}$ Pa s, b = 10 and T_{adi} is the temperature on the adiabat. For simplicity, we assume a Newtonian rheology and do not include a dependence on strain rate, consistent with the negligible strength of anisotropy in the main part of the lower mantle[50]. The density at the surface is $\rho_0 = 3300$ kg m^{-3}, and the compressibility $\kappa = 4.2 \times 10^{-12}$ Pa^{-1}, leading to a density of approximately 5560 kg m^{-3} at the core-mantle boundary, which is consistent with PREM[51] (but does not take into account density jumps at major phase transitions). The thermal expansivity is depth-dependent following the relation $\alpha_{thermal} = \alpha_{surface} \exp(-z/z_0)$, similar to the profile computed be Steinberger and Calderwood[52], but again not taking into account discontinuities at phase transitions. In this expression, the thermal expansivity at the surface is $\alpha_{surface} = 3.5 \times 10^{-5}$ K^{-1}, z is the depth and $z_0 = 2900$ km is the maximal depth of the model. This leads to a thermal expansivity of $\alpha_{thermal} = 1.3 \times 10^{-5}$ K^{-1} at the core-mantle boundary. We use a specific heat C_p = 1200 J kg^{-1} K^{-1}, and investigate the effects of thermal conductivity (k) for the lower mantle on the development and destabilization of the basal thermal boundary layer, and concomitant thermodiffusion. In the present examples we consider an upper limit of 8.5 W m^{-1} K^{-1} for the thermal conductivity after Ammann et al.[53] and lower limit of 4 W m^{-1} K^{-1} after Kavner and Rainey[54].

We use a value for α_o of 2.9 for modeling thermodiffusion in the vicinity of the CMB that is consistent with our experimental results for FeNi alloy melts possibly containing a small amount of a light element such as S. We consider this as a lower, and thus conservative, value for α_o in light of Kincaid et al.'s[55] contention that α_o increases with density. We do not anticipate that α_o will increase by much given that the density of molten iron increases by less than a factor of two between atmospheric and CMB pressures[49]. Likewise, co-author D. Lacks has performed MD simulations of thermodiffusion in magnesiosilicate liquids (unpub. results) showing that α_o for Mg is nearly constant between 0 and 25 GPa and 3500 – 4500 K, while α_o for Si and O increase by a factor of 2-3. Finally, we consider a range in Fe self-diffusivity for core-mantle boundary conditions, e.g., 1 x 10^{-9} to 1.5 x 10^{-8} m^2 s^{-1}, broadly consistent with extrapolations of Dobson's[56] free volume model and molecular dynamics simulations of Alfe et al.[57]. Lastly, we constrain the melting temperature of the FeNi alloy by the solidus of Morard et al.[49] for a typical core liquid containing Ni plus some light elements. The melting curve is given by the Simon-Gatzel equation, where

$$T_M = T_{M0} (P_M/a + 1)^{1/c} \qquad \text{(S-7)}$$

with T_{M0} = 1478 K, a = 10 GPa, c = 3.3 and the index M indicating melting temperature T or pressure P. In the 2-D ASPECT models the equations for thermodiffusion are only solved if the temperature is above the solidus, otherwise any existing anomalies in the concentration of ^{57}Fe are only advected using the velocity obtained by solving the mass and momentum conservation equations. As an alternative, we consider the possibility that the diffusion length scale is limited to only a few 10's of km if this is the limit of core liquid infiltration above the CMB. This analysis explores in more detail the interdependence of D_{Fe} and k on Fe isotope fractionation by thermodiffusion.

To make sure that we resolve the fractionation process accurately both in space and in time, we limit the time step to a maximum of 500,000 years (in addition to the constraint imposed by the Courant–Friedrichs–Lewy condition), and we adaptively refine the mesh wherever δ^{57}Fe exceeds ±4 x 10^{-3} ‰. This leads to a mesh cell size of less than 1.5 km in regions with anomalies in ^{57}Fe (and around 25 km in the rest of the domain) (see Fig. S7). In addition, we use a nonlinear solver, iterating over the advection and Stokes equations until convergence is reached. To put the time step size in perspective, the diffusion time scale across one mesh

cell $\tau = d^2/(\pi^2 D_{Fe})$ with d = 1.5 km and $D_{Fe} = 2.5 \times 10^{-9}$ m^2 s^{-1} is approximately τ = 3 Ma, so that at least 6 time steps are executed in the time it takes material to diffuse across one cell.

1-D Analysis of fractionation in a stationary boundary layer over time

We will start out by analyzing how the isotopic composition of the thermal boundary layer at the base of the mantle evolves over time, depending on the length scale that iron can infiltrate into the mantle and the relevant material properties of the lower mantle, most notably the thermal conductivity and the self-diffusivity of Fe. The thermal conductivity controls how fast the thermal boundary layer grows, and accordingly, the temperature gradient that drives isotopic fractionation. The self-diffusivity controls how fast iron isotopes fractionate under a given temperature gradient. To study the influence of these parameters, we run 1-D models using the setup given above, but without considering advection of material or heat. This is a computationally inexpensive method that allows us to investigate how the boundary layer evolves before it becomes unstable.

In a first set of models, we allow thermodiffusion to operate anywhere in the thermal boundary layer where the temperatures are above the iron solidus. This represents an extreme case, where core liquids are permitted to infiltrate up to a few hundreds of kilometers into the lower mantle. In this case, the first anomalies develop in a thin layer just above the core-mantle boundary that then grows over time as the temperature profile relaxes and the depth range over which the Fe alloy is molten increases. Fig. S7 shows an example with a thermal conductivity of k = 4 W m^{-1} K^{-1} and a self-diffusion of $D_{Fe} = 2.5 \times 10^{-9}$ m^2 s^{-1}. Because the heavier iron isotopes preferentially migrate toward lower temperatures, the region where iron is liquid becomes progressively enriched in ^{57}Fe (Fig. S7). Isotopic fractionation in this region approaches 0.05 ‰, representing only about 0.2% of the isotopic fractionation possible if the process were able to run to steady state.

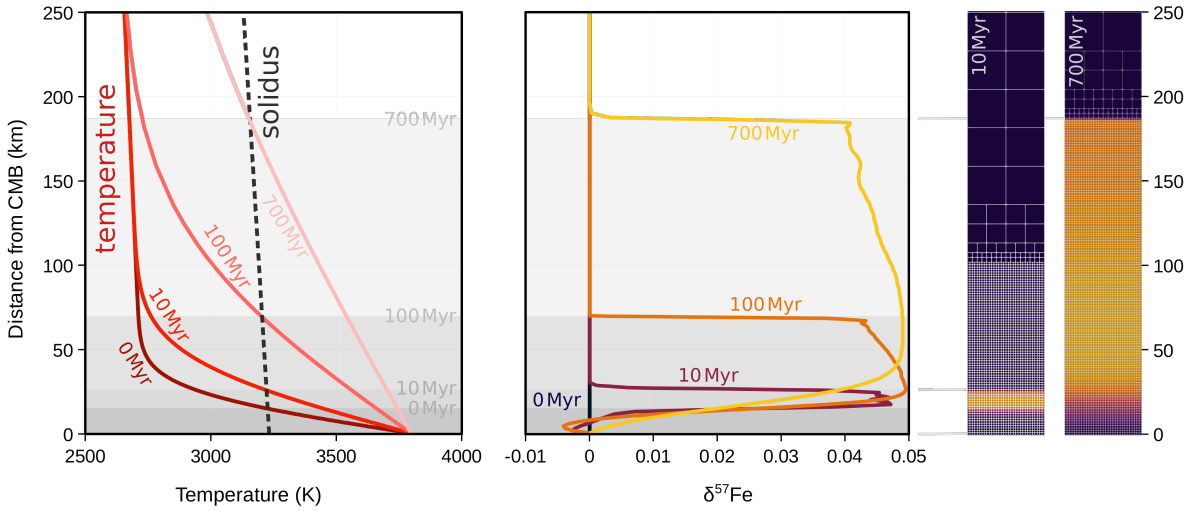

Figure S7. Evolution of the temperature (left), the δ^{57}Fe anomalies (center) and the mesh cells of the numerical model (right) across the thermal boundary layer above the core-mantle boundary (CMB) over the first 700 Myr of model evolution, before the plume starts to rise. The model uses a thermal conductivity of k = 4.0 W m^{-1} K^{-1} and D_{Fe} = 2.5 x 10^{-9} m^2 s^{-1}. (Left) Red solid lines show the temperature in the model at different times, as indicated by the labels; the dashed black line shows the iron solidus[49]. The initial temperature profile (0 Myr) corresponds to a thermal boundary layer with an age of 5 million years (computed using the half-space cooling model) imposed on top of an adiabatic temperature profile. (Center) Yellow-to-black solid lines show the evolution of the δ^{57}Fe anomalies, starting from a uniform distribution of δ^{57}Fe = 0 at 0 Myr. Light gray boxes in the background in the left and center panels mark the intersection of temperature and solidus at different model times, highlighting the depth ranges where fractionation of iron isotopes can occur.

In an alternative scenario, we consider thermodiffusion constricted to a few 10's of kms above CMB (Fig. S8). This is consistent with core liquid infiltration being more restricted and comparable to the scales of core – mantle interaction governed by grain boundary diffusion[58,59], capillary action[44,60,61] and stress[62]. There are two important consequences of more limited infiltration of core liquids. Firstly, given the shorter diffusion distance for isotopic fractionation by thermodiffusion, the liquids will approach steady-state more quickly. Secondly, given that temperatures and gradients in temperature are highest nearest the CMB, the rate of fractionation and thermal diffusion potential are also higher.

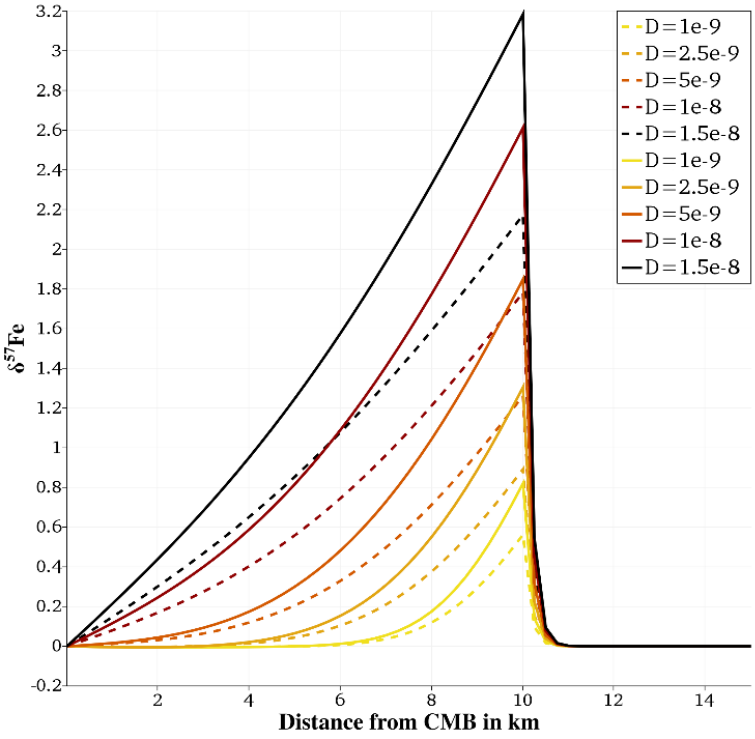

Figure S8. 1-D models of thermodiffusion in the thermal boundary layer. The profile shows the lowermost 10 km of the mantle after 100 Myrs of model evolution. Each line represents one model: solid lines use a thermal conductivity of k = 4 W m^{-1} K^{-1}, dashed lines use k = 8.5 W m^{-1} K^{-1}. The color of each line indicates the value of the Fe self-diffusivity, D_{Fe} (in m^2 s^{-1}).

We illustrate these effects in a set of 1-D models for thermal conductivities (k) of 4.0 and 8.5 W m^{-1} K^{-1}, and D_{Fe} ranging from 10^{-9} to 1.5 x 10^{-8} m^2 s^{-1}, where thermodiffusion is restricted to 10 km above the CMB. Fig. S8 shows that within this thin layer, isotopic fractionation can exceed 3.0 ‰ δ^{57}Fe in 100 Myrs. The smaller the thermal conductivity and the larger the iron self-diffusivity, the larger the fractionation that occurs in a given time interval. Our models illustrate the potential for the basal layer directly above the CMB to become isotopically heavy on geologically reasonable timescales by virtue of the steep temperature gradients. The total flux of heavy Fe across the core-mantle boundary in this case is not significantly different from that in the model that permits thermodiffusion to operate on length scales an order of magnitude larger, but the isotopic fractionation is markedly greater, principally because the diffusion distance is shorter and temperature gradients steeper, other factors being equal.

2-D ASPECT simulations

In a second step, we use 2-D geodynamic models to track how isotopically fractionated material would be entrained by mantle plumes, and if it could be sampled by melting in the upper mantle. We let the models evolve until the boundary layer becomes unstable, and a plume rises to the surface (Fig S9). Using, again, the diffusion time scale τ yields an approximate diffusion distance of 30 km over that time span. In the first part of the model evolution, there is negligible motion of the mantle while the thermal boundary layer is growing (Fig. S9, left column), and all isotopic anomalies start to develop in a thin layer close to the core–mantle boundary where the temperature exceeds the iron solidus, as predicted in the 1-D model presented above.

After a few hundred Myrs, with the exact timing depending on the specific model parameters, the thermal boundary layer becomes unstable and a plume starts to rise, entraining the layer enriched in ^{57}Fe (Fig. S9, center panels). Note that the center of the plume samples the hottest, lowermost part of the thermal boundary layer that was adjacent to the core-mantle boundary, where the exchange with core liquid keeps the isotopic composition fixed to δ^{57}Fe = 0. Hence, the ascending plume exhibits a thin centerline with almost no enrichment in heavy iron isotopes, surrounded by a ring enriched in ^{57}Fe. This structure is preserved as the plume rises and approaches the surface (Fig. S9, right column), where the δ^{57}Fe anomalies will be sampled in the melting process. Moreover, if thermodiffusion is restricted to the a few 10's of kilometers at the base of the mantle (Fig. S9, center row), heavy iron isotopes are concentrated near the top of the plume head and near the center of the plume tail.

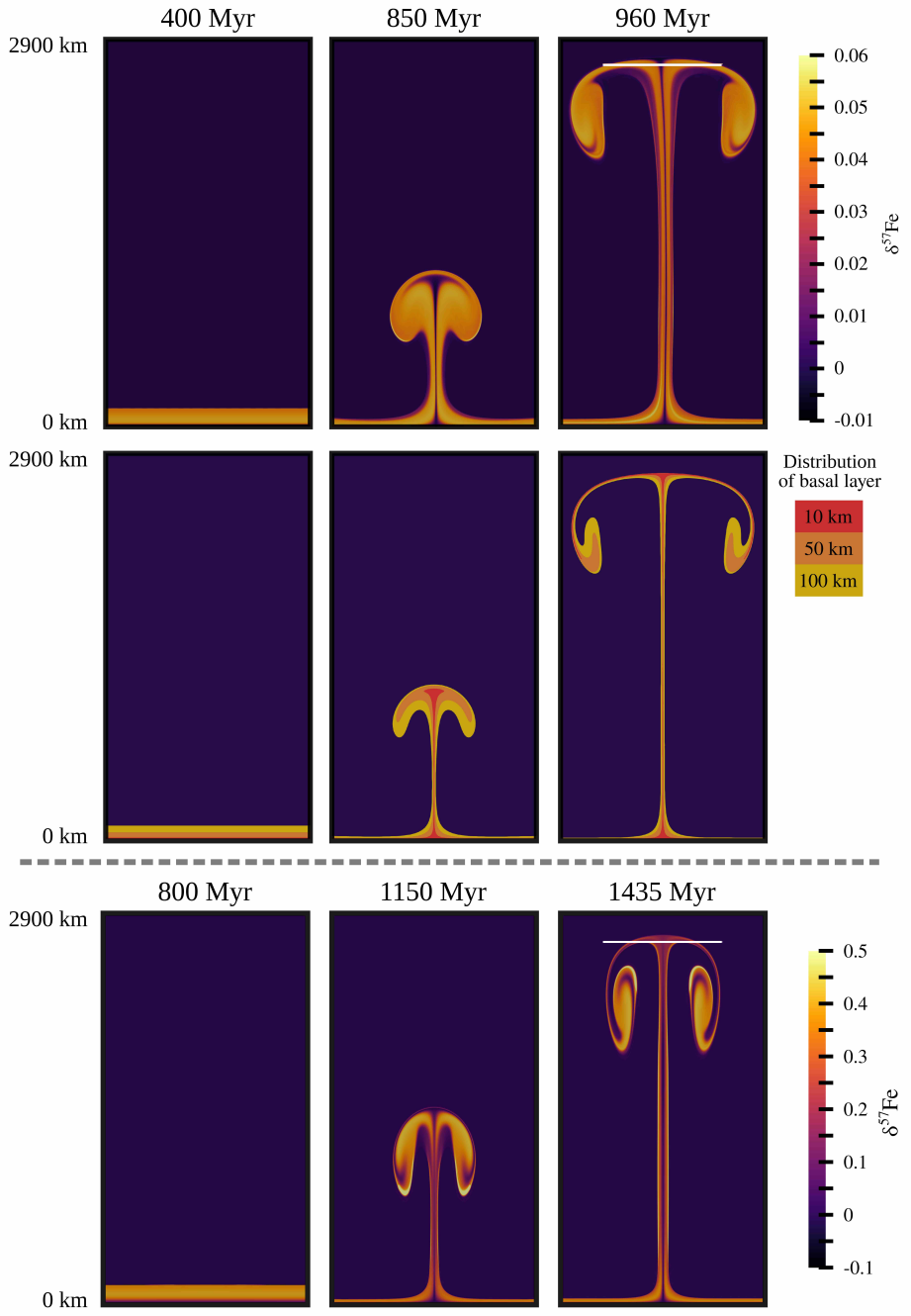

Figure S9. Evolution of the basal boundary layer developing into a plume simulated by our ASPECT geodynamic model. Only the center part of the models is shown. The top two rows of panels show the model with a thermal conductivity k = 8.5 W m^{-1} K^{-1} and D_{Fe} = 2.5 x 10^{-9} m^2 s^{-1}. The bottom row shows the model with k = 4 W m^{-1} K^{-1} and D_{Fe} = 10^{-8} m^2 s^{-1}. In the top and bottom rows, colors represent the δ^{57}Fe anomalies. Note that color scales are about an order of magnitude different in the top vs. the bottom row. The center row considers the possibility that thermodiffusion is constrained to the lowermost 10 (red area), 50 (orange area) or 100 (yellow area) kilometers of the mantle and tracks how such a layer would be distributed in a rising plume. The horizontal white lines in the top and bottom panels mark a depth of 200 km.

Varying material properties that can strongly effect isotopic fractionation, e.g. thermal conductivity and iron self-diffusivity, within reasonable limits do not drastically change the distribution of isotopically heavy material in the plume (compare Fig. S9 top and bottom). However, these parameters do change the magnitude of Fe isotopic fractionation. In the model with $k = 4$ W m^{-1} K^{-1} and $D_{Fe} = 10^{-8}$ m^2 s^{-1} (Fig. S9, bottom row), the δ^{57}Fe anomalies are about an order of magnitude larger, reaching values of up to 0.5‰.

These 2-D plume models show that mantle plumes entraining the isotopically heavy boundary layer are a feasible mechanism to transport this composition to the asthenosphere. The details of the distribution of isotopic heterogeneity may change for more realistic plume models, for example, in three dimensions and with a more realistic rheology including viscosity changes at major phase transitions, dislocation creep or the dependence on an evolving grain size. However, we are confident that the models presented here capture the expected magnitude of the δ^{57}Fe anomaly developing within the thermal boundary layer at the base of the mantle over time and the general pattern in the distribution of ^{57}Fe in an ascending plume that originates from the vicinity of the core-mantle boundary.

Implications

The modeling results presented here show that the thermodiffusion potential is capable of producing a large isotopic effect near the CMB, and that this fractionated material will be entrained by plume upwelling mostly concentrated near the plume axis but potentially more widely dispersed within the plume head. However, given the small fraction of core material involved, dilution by the silicate mantle is likely to mask the isotopic effects except where the fractionation is greatest. The most favorable conditions are thus near the plume axis and where core liquid infiltration is limited to a few tens of kilometers. Drawing on the model results presented in Fig. S8 for the most favorable conditions (low K and high D_{Fe}), addition of 0.2 wt. % Fe from the core with δ^{57}Fe = 2.55 ‰ to silicate mantle with 7.7 wt. % Fe and δ^{57}Fe = 0 ‰ yields a bulk mixture with δ^{57}Fe of +0.064 ‰. If the core contribution is increased to 0.8 wt. %, the bulk δ^{57}Fe would be +0.240 ‰. These small additions of core material are thus sufficiently large to elevate the Fe isotopic composition to well above measurable levels, while not exceeding limits of core additions constrained by W isotopes[15,16]. However, it is not currently known how well coupled Fe and W are during core – mantle interaction or partial melting, reactive transport and metasomatic processes in the

upper mantle given expected differences in compatibility in mantle silicates, fluids and sulfides[63].

Finally, in Fig. S-10 we consider the ramifications of mixing lower mantle boundary layer material with mantle reservoirs equivalent in volume to the whole mantle, upper mantle (down to 660 km) and asthenosphere (down to 410 km) over geologic time. These calculations use the results of our 1-D models, quantifying the flux of heavy iron isotopes across the core-mantle boundary. Our estimates assume the addition of basal material containing 0.2, 0.5 and 0.8 wt. % core material every 100 Myrs up to the age of the Earth having an average δ^{57}Fe of 2.6 ‰ and 3.9 ‰ (Fig. S8 for thermodiffusion models with k = 4.0 and 8.5 W m^{-1} K^{-1}, respectively, and D_{Fe} = 1.5 x 10^{-8} m^2 s^{-1}. These calculations show that δ^{57}Fe barely reaches 0.02 ‰ if the basal layer is mixed into the whole mantle or even the entire upper mantle, but could impart a positive shift in δ^{57}Fe exceeding 0.05 ‰ to the asthenosphere. This is noteworthy given this is approximately the mean value of peridotites shown in Fig. S1. This correspondence could be explained if the asthenosphere sampled by mid-ocean ridge magmatism is principally plume-fed as proposed by Morgan et al.[64].

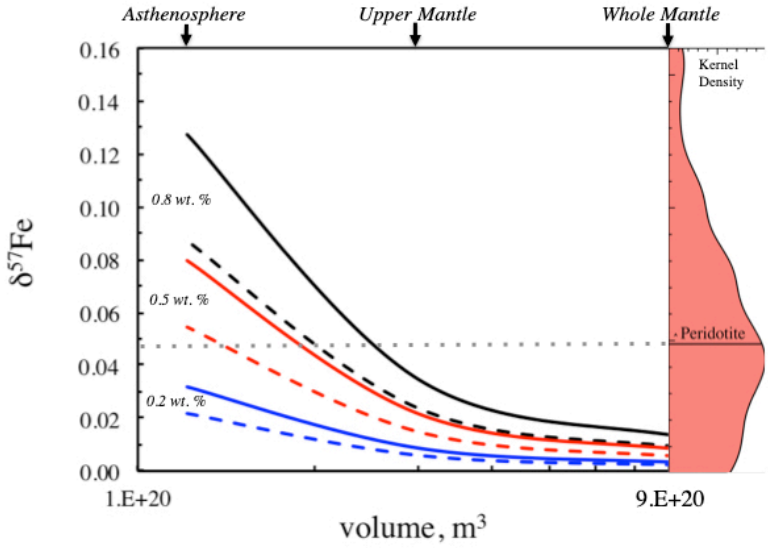

Figure S10. Fe isotope composition for mantle reservoirs today resulting solely from mixing of upwelling plume material from a basal layer enriched in heavy Fe over the history of the Earth. The mixing calculations assume addition of this basal material containing 0.2, 0.5 and 0.8 wt. % of core material every 100 Myrs with average isotopic composition taken from Fig. S8 for a D_{Fe} = 1.5 x 10^{-8} m^2 s^{-1}. Solid curves are for a lower mantle thermal conductivity (k) of 4.0 W m^{-1} K^{-1} and dashed curves are for 8.5 W m^{-1} K^{-1}. The kernel density distribution for mantle peridotites is taken from Fig. S1.

Code availability. The version of ASPECT we used to compute the geodynamic models is available online (https://github.com/jdannberg/aspect/commits/iron_fractionation), and all input files required to reproduce our computations, together with instructions for how to run them, are provided in a separate repository (https://github.com/jdannberg/SI-data-thermodiffusion).

References

1. Beard, B. L. & Johnson, C. M. Inter-mineral Fe isotope variations in mantle-derived rocks and implications for the Fe geochemical cycle. *Geochim. Cosmochim. Acta* **68,** 4727–4743 (2004).
2. Poitrasson, F., Halliday, A. N., Lee, D.-C., Levasseur, S. & Teutsch, N. Iron isotope differences between Earth, Moon, Mars and Vesta as possible records of contrasted accretion mechanisms. *Earth Planet. Sci. Lett.* **223,** 253–266 (2004).
3. Weyer, S. *et al.* Iron isotope fractionation during planetary differentiation. *Earth Planet. Sci. Lett.* **240,** 251–264 (2005).
4. Williams, H. *et al.* Systematic iron isotope variations in mantle rocks and minerals: The effects of partial melting and oxygen fugacity. *Earth Planet. Sci. Lett.* **235,** 435–452 (2005).
5. Dauphas, N. *et al.* Magma redox and structural controls on iron isotope variations in Earth's mantle and crust. *Earth Planet. Sci. Lett.* **398,** 127–140 (2014).
6. Sossi, P. A., Nebel, O. & Foden, J. Iron isotope systematics in planetary reservoirs. *Earth Planet. Sci. Lett.* **452,** 295–308 (2016).
7. Polyakov, V. B. Equilibrium iron isotope fractionation at core-mantle boundary conditions. *Science* **323,** 912–914 (2009).
8. Dauphas, N. *et al.* Iron isotopes may reveal the redox conditions of mantle melting from Archean to Present. *Earth Planet. Sci. Lett.* **288,** 255–267 (2009).
9. Craddock, P. R. & Dauphas, N. Iron isotopic compositions of geological reference materials and chondrites. *Geostand. Geoanalyt. Res.* **35,** 101–123 (2011).
10. Craddock, P. R., Warren, J. M. & Dauphas, N. Abyssal peridotites reveal the near-chondritic Fe isotopic composition of the Earth. *Earth Planet. Sci. Lett.* **365,** 63–76 (2013).
11. Teng, F.-Z., Dauphas, N., Huang, S. & Marty, B. Iron isotopic systematics of oceanic basalts. *Geochim. Cosmochim. Acta* **107,** 12–26 (2013).
12. Porcelli, D. & Halliday, A. N. The core as a possible source of mantle helium. *Earth Planet. Sci. Lett.* **192,** 45–56 (2001).
13. Humayun, M. Geochemical Evidence for Excess Iron in the Mantle Beneath Hawaii. *Science* **306,** 91–94 (2004).
14. Bouhifd, M. A., Jephcoat, A. P., Heber, V. S. & Kelley, S. P. Helium in Earth's early core. *Nature Geosci.* **6,** 982–986 (2013).
15. Mundl, A. *et al.* Tungsten-182 heterogeneity in modern ocean island basalts. *Science* **356,** 66–69 (2017).
16. Rizo, H. *et al.* 182W evidence for core-mantle interaction in the source of mantle plumes. *Geochem. Persp. Lett.,**11,*** 6–11 (2019).
17. Teng, F. Z., Dauphas, N. & Helz, R. T. Iron isotope fractionation during

magmatic differentiation in Kilauea Iki lava lake. *Science* **320,** 1620–1622 (2008).
18. Williams, H. M. & Bizimis, M. Iron isotope tracing of mantle heterogeneity within the source regions of oceanic basalts. *Earth Planet. Sci. Lett.* **404,** 396–407 (2014).
19. Teng, F.-Z., Dauphas, N., Helz, R. T., Gao, S. & Huang, S. Diffusion-driven magnesium and iron isotope fractionation in Hawaiian olivine. *Earth Planet. Sci. Lett.* **308,** 317–324 (2011).
20. Schoenberg, R. & Blanckenburg, F. V. Modes of planetary-scale Fe isotope fractionation. *Earth Planet. Sci. Lett.* **252,** 342–359 (2006).
21. Hin, R. C., Schmidt, M. W. & Bourdon, B. Experimental evidence for the absence of iron isotope fractionation between metal and silicate liquids at 1GPa and 1250-1300°C and its cosmochemical consequences. *Geochim. Cosmochim. Acta* **93,** 164–181 (2012).
22. Shahar, A. *et al.* Pressure-dependent isotopic composition of iron alloys. *Science* **352,** 580–582 (2016).
23. Liu, J. *et al.* Iron isotopic fractionation between silicate mantle and metallic core at high pressure. *Nature Comm.* **8,** 14377 (2017).
24. Elardo, S. M. & Shahar, A. Non-chondritic iron isotope ratios in planetary mantles as a result of core formation. *Nature Geosci.* **10,** 317–321 (2017).
25. Wang, K., Jacobsen, S. B., Sedaghatpour, F., Chen, H. & Korotev, R. L. The earliest Lunar Magma Ocean differentiation recorded in Fe isotopes. *Earth Planet. Sci. Lett.* **430,** 202–208 (2015).
26. Watson, E., Wark, D., Price, J. & Van Orman, J. Mapping the thermal structure of solid-media pressure assemblies. *Contrib Mineral Petrol.* **142,** 640–652 (2002).
27. Brenan, J. M. & Bennett, N. Soret separation of highly siderophile elements in Fe–Ni–S melts: Implications for solid metal–liquid metal partitioning. *Earth Planet. Sci. Lett.* **298,** 299–305 (2010).
28. Lesher, C. E., Pickering-Witter, J., Baxter, G. & Walter, M. Melting of garnet peridotite: Effects of capsules and thermocouples, and implications for the high-pressure mantle solidus. *Am. Mineral.* **88,** 1181–1189 (2003).
29. Liu, L. G. & Bassett, W. A. The melting of iron up to 200 kbar. *J. Geophys. Res.* **80,** 3777–3782 (1975).
30. Belshaw, N. S., Zhu, X. K., Guo, Y. & O'Nions, R. K. High precision measurement of iron isotopes by plasma source mass spectrometry. *Intern. J. Mass Spectro.* **197,** 191–195 (2000).
31. Beard, B. L. *et al.* Application of Fe isotopes to tracing the geochemical and biological cycling of Fe. *Chem. Geol.* **195,** 87–117 (2003).
32. Schoenberg, R. & Blanckenburg, von, F. An assessment of the accuracy of stable Fe isotope ratio measurements on samples with organic and inorganic matrices by high-resolution multicollector ICP-MS. *Intern. J. Mass Spectro.* **242,** 257–272 (2005).
33. Dauphas, N. *et al.* Chromatographic separation and multicollection-ICPMS analysis of iron. investigating mass-dependent and -independent isotope effects. *Anal. Chem.* **76,** 5855–5863 (2004).
34. Young, E. D., Galy, A., Acta, H. N. G. E. C.2002. Kinetic and equilibrium mass-dependent isotope fractionation laws in nature and their geochemical and cosmochemical significance. *Earth Planet. Sci. Lett.* **66,** 1095–1104 (2002).
35. Williams, H. M. *et al.* Fe isotope fractionation in iron meteorites: New insights

into metal-sulphide segregation and planetary accretion. *Earth Planet. Sci. Lett.* **250,** 486–500 (2006).

36. Shahar, A. *et al.* Sulfur-controlled iron isotope fractionation experiments of core formation in planetary bodies. *Geochim. Cosmochim. Acta* **150,** 253–264 (2015).
37. Severinghaus, J. P., Grachev, A. & Battle, M. Thermal fractionation of air in polar firn by seasonal temperature gradients. *Geochem. Geophys. Geosys.* **2,** (2001).
38. Lesher, C. E. & Walker, D. Solution properties of silicate liquids from thermal diffusion experiments. *Geochim. Cosmochim. Acta* **50,** 1397–1411 (1986).
39. Lacks, D. J. *et al.* Isotope fractionation by thermal diffusion in silicate melts. *Phys. Rev. Lett.* **108,** 065901–5 (2012).
40. Huang, F. *et al.* Isotope fractionation in silicate melts by thermal diffusion. *Nature* **464,** 396–400 (2010).
41. Heister, T., Dannberg, J., Gassmöller, R. & Bangerth, W. High accuracy mantle convection simulation through modern numerical methods – II: realistic models and problems. *Geophy. J. Int.* **210,** 833–851 (2017).
42. Bangerth, W., Dannberg, J., Gassmoeller, R., Heister, T. & others. ASPECT: Advanced Solver for Problems in Earth's ConvecTion, User Manual. *Computational Infrastructure for Geodynamics (2018).* Available at: https://aspect.geodynamics.org. (Accessed: 11th February 2020).
43. Guermond, J.-L., Pasquetti, R. & Popov, B. Entropy viscosity method for nonlinear conservation laws. *J Computation. Phys.* **230,** 4248–4267 (2011).
44. Otsuka, K. & Karato, S.-I. Deep penetration of molten iron into the mantle caused by a morphological instability. *Nature* **492,** 243–246 (2012).
45. Shi, C. Y. *et al.* Formation of an interconnected network of iron melt at Earth's lower mantle conditions. *Nature Geosci.* **6,** 971–975 (2013).
46. Liu, J., Li, J., Hrubiak, R. & Smith, J. S. Origins of ultralow velocity zones through slab-derived metallic melt. *Proc. Natl. Acad. Sci.* **113,** 5547–5551 (2016).
47. Williams, Q. & Garnero, E. J. Seismic evidence for partial melt at the base of Earth's mantle. *Science* **273,** 1528–1530 (1996).
48. Buffett, B. A. & Seagle, C. T. Stratification of the top of the core due to chemical interactions with the mantle. *J. Geophys. Res.* **115,** B04407–10 (2010).
49. Morard, G. *et al.* Melting of Fe–Ni–Si and Fe–Ni–S alloys at megabar pressures: implications for the core–mantle boundary temperature. *Phys. Chem. Minerals* **38,** 767–776 (2011).
50. Karato, S.-I. Rheology of the deep upper mantle and its implications for the preservation of the continental roots: A review. *Tectonophysics* **481,** 82–98 (2010).
51. Dziewonski, A. M. & Anderson, D. L. Preliminary reference Earth model. *Phys. Earth Planet. Int.* **25,** 297–356 (1981).
52. Steinberger, B. & Calderwood, A. R. Models of large-scale viscous flow in the Earth's mantle with constraints from mineral physics and surface observations. *Geophy. J. Int.* **167,** 1461–1481 (2006).
53. Ammann, M. W. *et al.* Variation of thermal conductivity and heat flux at the Earth's core mantle boundary. *Earth Planet. Sci. Lett.* **390,** 175–185 (2014).
54. Kavner, A. & Rainey, S. G. in *Deep Earth Physics and Chemistry of the Lower Mantle and Core* (eds. Terasaki, H. & Fischer, R. A.) Geophysical Monograph **217,** 31–42 (Wiley Online Library, 2016).
55. Kincaid, J. M., Cohen, E. G. D. & de Haro, M. L. The Enskog theory for

multicomponent mixtures. IV. Thermal diffusion. *J. Chem. Phys.* **86,** 963–975 (1998).
56. Dobson, D. P. Self-diffusion in liquid Fe at high pressure. *Phys. Earth Planet. Int.* **130,** 271–284 (2002).
57. Alfè, D. & Kresse, G. Structure and dynamics of liquid iron under Earth's core conditions. *Phys. Rev. B* **61,** 132–142 (2000).
58. Hayden, L. A. & Watson, E. B. A diffusion mechanism for core–mantle interaction. *Nature* **450,** 709–711 (2007).
59. Crispin, K. L., Saha, S., Morgan, D. & Van Orman, J. A. Diffusion of transition metals in periclase by experiment and first-principles, with implications for core–mantle equilibration during metal percolation. *Earth Planet. Sci. Lett.* **357-358,** 42–53 (2012).
60. Poirier, J.-P. Core-infiltrated mantle and the nature of the D" layer. *J. Geomagn. Geoelectr.* **45,** 1221–1227 (1993).
61. Goarant, F., Guyot, F., Peyronneau, J. & Poirier, J.-P. High‐pressure and high‐temperature reactions between silicates and liquid iron alloys, in the diamond anvil cell, studied by analytical electron microscopy. *J. Geophys. Res.* **97,** 4477–4487 (1992).
62. Kanda, R. V. S. & Stevenson, D. J. Suction mechanism for iron entrainment into the lower mantle. *Geophys. Res. Lett.* **33,** 19581 (2006).
63. Luguet, A. *et al.* Enriched Pt-Re-Os Isotope Systematics in Plume Lavas Explained by Metasomatic Sulfides. *Science* **319,** 453 (2008).
64. Morgan, J. P., Hasenclever, J. & Shi, C. New observational and experimental evidence for a plume-fed asthenosphere boundary layer in mantle convection. *Earth Planet. Sci. Lett.* **366,** 99–111 (2013).